

Supporting Information

Strain Engineering and Raman Spectroscopy of Monolayer Transition Metal Dichalcogenides

A. M. Dadgar^{1,2}, D. Scullion³, K. Kang⁴, D. Esposito⁵, E-H. Yang⁴, I. P. Herman⁶, M. A. Pimenta⁷, E-J. G. Santos⁸, A. N. Pasupathy²

¹ Department of Mechanical Engineering, Columbia University, New York, NY 10027, USA

² Physics Department, Columbia University, New York, NY, 10027, USA

³ School of Mathematics and Physics, Queens University, Belfast, BT7 1NN, UK

⁴ Department of Mechanical Engineering, Stevens Institute of Technology, Castle Point on the Hudson, Hoboken, NJ, USA

⁵ Department of Chemical Engineering, Columbia University - New York, NY 10027, USA

⁶ Department of Applied Physics and Applied Mathematics, Columbia University, New York - NY 10027, USA

⁷ Department of Physics, Universidade Federal de Minas Gerais (UFMG), Brazil

⁸ School of Chemistry and Chemical Engineering, Queen's University - Belfast, BT9 5AL, UK

Strain Method

Our samples are monolayer flakes with a typical size of 10 μm . Direct stretching of the flake along the strain direction requires exceptionally precise control of the displacement, which is not easily achieved in a simple mechanical apparatus. We thus use an apparatus to bend the substrate in which the flakes are embedded as a simple way to achieve controllable strains. Areas above the neutral axis of the substrate undergo tensile strain while areas below the neutral axis experience compressive strain. It is typically assumed that the substrate bends in a circular arc upon bending. While reasonable at small strains, this approximation is incorrect at higher strains. In order to resolve this issue, we solve the Euler-Bernoulli's equation ¹ for our experimental geometry to compute strain as a function of vertical displacement. We approximate the substrate to be a fully elastic, linear and isotropic material that obeys Hooke's Law.

Figure S1-a is the static free body diagram of the substrate under extra neutral axis bending. The ends of the beam (between A and B as well as between C and D in the figure S1-b) are cantilevers, with a center region between B and C undergoing pure bending. We first consider the center region and solve Euler-Bernoulli's equation for the vertical position of the substrate y as a function of the horizontal position x :

$$EI \frac{d^2y}{dx^2} = M = Pa \quad (1)$$

where E is Young's modulus of elasticity, I is cross sectional moment of inertia, M is bending moment and P is the vertical load on the system. Since this region is under pure bending, the bending moment, $M = Pa$ is position independent (figure S1-c-right and S1-b-right). As a consequence, the strain in this region is also position independent. This property of the technique is highly desirable to achieve uniform strain on the sample and is the main reason for choosing this geometry. Solving this differential equation and applying boundary conditions, the final

equation of the beam in the center region is:

$$Ely = \frac{1}{2}Pax^2 - \frac{1}{2}Pabx \quad (2)$$

In the cantilever region, the bending moment is position dependent: $M = Px$ which is shown in figure S1-c,-left panel.

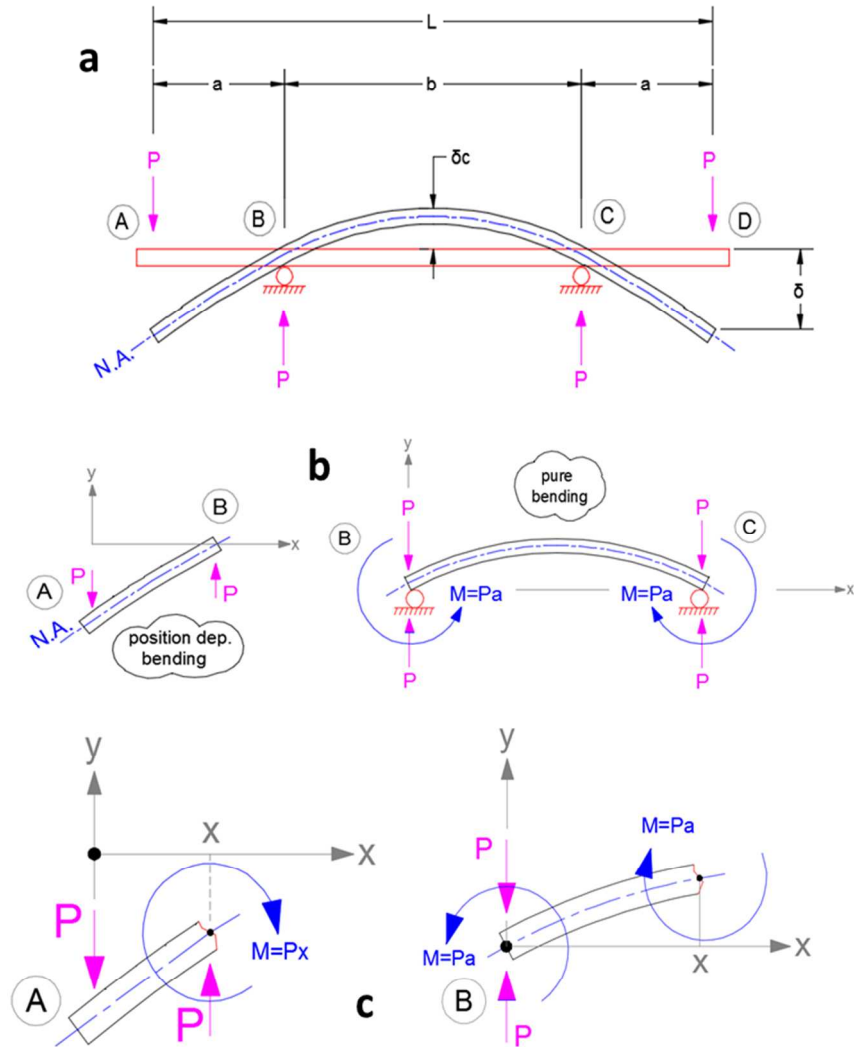


Figure S1 – Statics equilibrium of beam under extra neutral axis bending. (a) Statics of the whole beam under bending. (b) Beam is divided into two sections: (left) cantilever sections and (right) center section. (c) Details of loading at an arbitrary point of these regions.

Solving the Euler-Bernoulli equation and applying the appropriate boundary conditions gives the deflection equation in this region:

$$EIy = \frac{1}{6}P(x^3 - a^3) - \frac{1}{2}Pa(x - a)(a + b) \quad (3)$$

Using this function, we can now relate δ the vertical displacement at $x = 0$ to the other parameters of the beam:

$$\delta = \frac{1}{6} \frac{Pa^2}{EI} (2a + 3b) \quad (4)$$

Meanwhile, the maximum stress σ in the center region can be calculated using Hooke's Law [1]: $\sigma = pat/2I$, where t is the thickness of the substrate. Re-writing Hooke's Law for the uniaxial stress case, we will have the strain relation $\epsilon = pat/2EI$. Combining this with equation (4), we get our desired relation – ϵ as a function of beam geometry and vertical displacement δ :

$$\epsilon = \frac{3t\delta}{a(3b+2a)} \quad (5)$$

By choosing a, b, t appropriately and controlling the vertical motion δ stepwise using a differential screw, we can apply linear stepwise strain to the flakes being studied.

The main remaining experimental challenge is to make a fully elastic springy material with a large elastic region which obeys the formula above. This is performed as described in the main text - we first measured the glass transition temperature T_g of different polymer materials and stacks. Then after encapsulating our semiconductor devices in our desired polymer, we heated it up to the annealing temperature $T_a = 0.97T_g$. The optimized annealing time was found to be $t_a = 60 \text{ min}$ for substrates with $t = 0.5 \text{ mm}$ thicknesses. We found that applying pressure of $P_a = 3 \text{ psi}$ during the annealing makes better re-crystallized substrates. Finally, very slow cooling at $r_a = 2 \text{ }^\circ\text{C/min}$ completes the substrate fabrication. These devices display an excellent match with equation (5)

Strength or Intensity of Raman Scattering

The intensity of the Raman response for a given light polarization can be determined from the Raman tensor \tilde{R} ²:

$$I \propto |\hat{e}_s^T \cdot \tilde{R} \cdot \hat{e}_i|^2$$

where \hat{e}_i and \hat{e}_s are the polarization directions of the incident and scattered light's electric field respectively. A typical cross polarization geometry is illustrated in Figure S2.

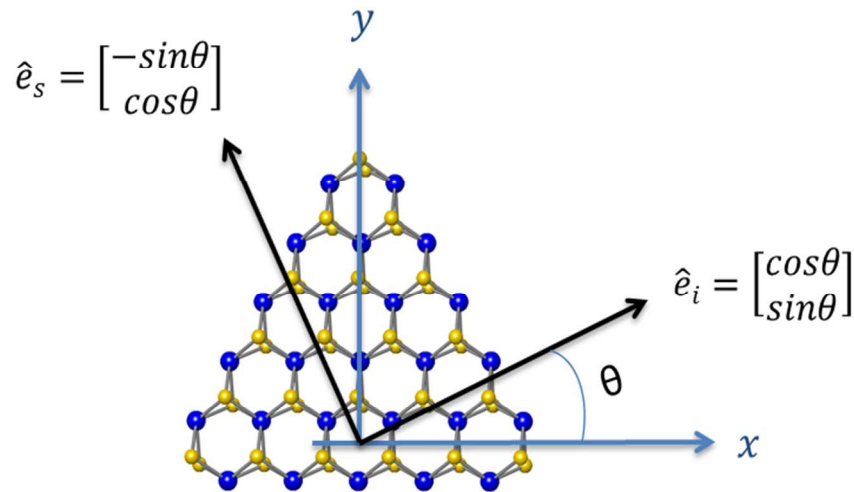


Figure S2 – Directions of incident and scattered light with respect to crystal's Cartesian coordinate systems. x- and y-directions represent zigzag and armchair directions respectively

When the incident laser light is applied in either the zigzag or armchair direction of a single layer orthorhombic crystal, the Raman tensor for the A' mode is a diagonal matrix which can be written as follows:

$$R = \begin{bmatrix} a & 0 \\ 0 & b \end{bmatrix}$$

Consequently the Raman intensity of the A' mode in the cross polarization geometry shown in figure S2 is:

$$I_{XY}^A \propto \left| [\cos\theta \quad \sin\theta] \begin{bmatrix} a & 0 \\ 0 & b \end{bmatrix} \begin{bmatrix} -\sin\theta \\ \cos\theta \end{bmatrix} \right|^2 = |(b-a)\cos\theta\sin\theta|^2$$

This implies that when the incident light is along the crystal's principal directions, $\theta = 0^\circ$ or $\theta = 90^\circ$ (zigzag or armchair directions in figure S2), the A' mode is not observed in the cross polarization geometry.

In the presence of larger strains the orthorhombic symmetry of the crystal is lowered to triclinic, in which the corresponding Raman tensor for the A' mode is a non-diagonal matrix:

$$R = \begin{bmatrix} a & c \\ -c & b \end{bmatrix}$$

in this case the Raman intensity of the A' mode is always nonzero :

$$I_{XY}^A \propto \left| [\cos\theta \quad \sin\theta] \begin{bmatrix} a & c \\ -c & b \end{bmatrix} \begin{bmatrix} -\sin\theta \\ \cos\theta \end{bmatrix} \right|^2 = |(b-a)\cos\theta\sin\theta + c|^2 \neq 0$$

This might be the reason that we observe A' mode at highly-strained WS_2 samples only. Subsequently, for WSe_2 , there might be also possible contributions of the A' mode at higher strains, but we could not observe this because the A' and E' modes are accidentally degenerate in this material.

General Theoretical Methods:

Theoretical calculations were performed using the DFT formalism as implemented in the Vienna

ab initio simulation package (VASP)^{3, 4}. For the calculations of phonon modes, PHONON^{5, 6} was used. A $2 \times 2 \times 1$ supercell was used for these calculations. This was increased to $3 \times 3 \times 1$ and there was no appreciable difference found in the Γ -point phonon frequencies. For the calculations of Raman band frequency, PHONON was used implementing the PEAD method. The PBE functional⁷ was used along with the plane-wave cutoff of 800 eV combined with the projector-augmented wave (PAW) method^{8, 9}. Atoms were allowed to relax under the conjugate-gradient algorithm until the forces acting on the atoms were less than 10^{-8} eV/Å. The self-consistent field (SCF) convergence was also set to 10^{-8} eV. We employ an orthorhombic cell to apply uniaxial strain. Relaxed lattice constants were found to be $a = 3.187\text{Å}$, $b = 5.52\text{Å}$ for monolayer WS₂ and $a = 3.319\text{Å}$, $b = 5.750\text{Å}$ for WSe₂. A 20Å vacuum space was used to restrict interactions between images. A $182 \times 12 \times 1$ gamma-centered k-grid was used to sample the Brillouin Zone for both systems. Our calculations neglect the effect of the substrate which can influence the electron-phonon coupling via screening.

First-Principle Ab Initio Calculations

Theoretical calculations were carried out on the $n \times n$ ($n=1,2,3$) orthorhombic cells for both WS₂ and WSe₂ (see Figure S3). The lattice constants were found to be $a=3.187\text{Å}$, $b=5.520\text{Å}$ for WS₂ and $a=3.319\text{Å}$, $b=5.750\text{Å}$ for WSe₂. A 25Å vacuum space was used in all calculations. Strain was applied along of the armchair direction. There was no observed geometric transition from an orthorhombic unit cell to a monoclinic unit cell after the strain was applied. Even though, the high magnitudes of strain ($>3.0\%$) can incidentally change the local symmetry of the atoms from D_{3h} to a lower-symmetry group.

At zero strain, under cross polarization, both the P1 and A' mode are suppressed. When strain is

applied to the system ($\sim 3.0\%$), we see an increment of the intensity from zero to 5×10^{-6} a.u. for the A' mode and 1×10^{-8} a.u. for the P_1 mode. The large difference in intensities between both modes (500 times) indicates that the P_1 mode is incredibly weak relative to A' , which is almost at the numerical accuracy of the calculation. As a matter of fact, just the A' mode is experimentally observed at the high-strain regime (figure 3a in the main text), which fully corroborates the vibrational analysis performed. This suggests that large strain can indeed change the selection rules for the modes, even though their weak intensities may not be measured within the limit of resolution of the analyzer.

In general, major features of the strain dependence of the peak positions and intensities are in good agreement with our theoretical calculations. A comparison of the broad trends in the mode frequencies in WS_2 and WSe_2 can be explained on the basis of the difference between the chalcogen masses and the difference in the ionicity of the metal-chalcogen bond. We note that the detailed features of the spectra such as the splitting of the E' mode with strain depend on the details of the anharmonicity in the interatomic potentials.

Growth of Monolayer WS_2 on SiO_2 Substrates

The sample was comprised of a tungsten source carrier chip (5nm WO_3 thin film on 90 nm SiO_2) and bare SiO_2/Si substrate (90 nm thick SiO_2 , WRS materials). Tungsten oxide (WO_3 , 99.99%, Kurt J. Lesker) was deposited on SiO_2 via electron beam evaporation. The tungsten source chip was covered, in face-to-face contact, by a bare SiO_2/Si substrate as the growth substrate. The sample was loaded into the center of a 3" diameter and 1 m long quartz tube (MTI Corp.), and a ceramic boat with 0.8 g of sulfur powder (99.98%, Sigma-Aldrich) was located upstream in the quartz tube. After loading, the ambient gas of the tube was purged out via mechanical pump to

the base pressure of 400 mTorr. The furnace was heated to 700 °C at a 20 °C/min ramping rate and then to 900 °C at 5 °C/min. 60 sccm of Ar gas (5.0 UH purity, Praxair) was introduced at 150 °C (increasing temperature) to reduce moisture inside of the tube and closed at 600 °C (decreasing temperature). Hydrogen (40 sccm, 5.0 UH purity, Praxair) gas was supplied to improve WO₃ reduction from 700 °C (increasing temperature) to 600 °C (decreasing temperature). The growth pressure was 7 Torr. After 25 min at 900 °C, the furnace was cooled down to room temperature.

Growth of Monolayer WSe₂ on a SiO₂ Substrates

The sample was comprised of a tungsten source carrier chip (5nm WO₃ thin film on 90 nm SiO₂) and bare SiO₂/Si substrate (90 nm thick SiO₂, WRS materials). Tungsten oxide (WO₃, 99.99%, Kurt J. Lesker) was deposited on SiO₂ via electron beam evaporation. The tungsten source chip was covered, in face-to-face contact, by a bare SiO₂/Si substrate as the growth substrate. The sample was loaded into the center of a 2" diameter and 24" long quartz tube (MTI Corp.), and a ceramic boat with 0.8 g of selenium powder (99.99%, Sigma-Aldrich) was located upstream in the quartz tube. After loading, the ambient gas of the tube was purged out via mechanical pump to the base pressure of 100 mTorr. The furnace was heated to 700 °C at a 20 °C/min ramping rate and then to 900 °C at 5 °C/min. 20 sccm of Ar gas (5.0 UH purity, Praxair) was introduced at 150 °C (increasing temperature) to reduce moisture inside of the tube and closed at 600 °C (decreasing temperature). Hydrogen (10 sccm, 5.0 UH purity, Praxair) gas was supplied to improve WO₃ reduction from 700 °C (increasing temperature) to 600 °C (decreasing temperature). The growth pressure was 1 Torr. After 25 min at 900 °C, the furnace was cooled down to room temperature.

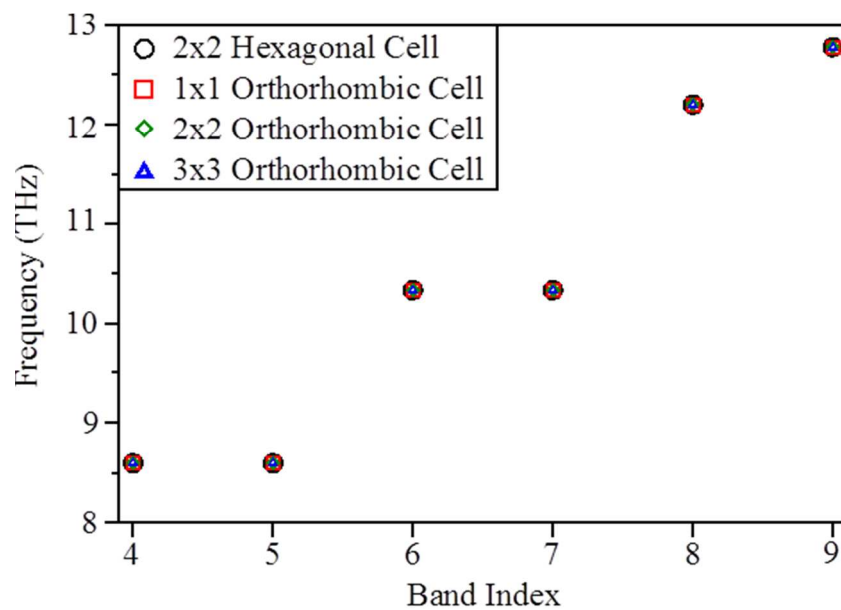


Figure S3 – Convergence of phonon frequencies with respect to the size of the supercell. As it can be seen, there is no change in the phonon frequency while changing the supercell size.

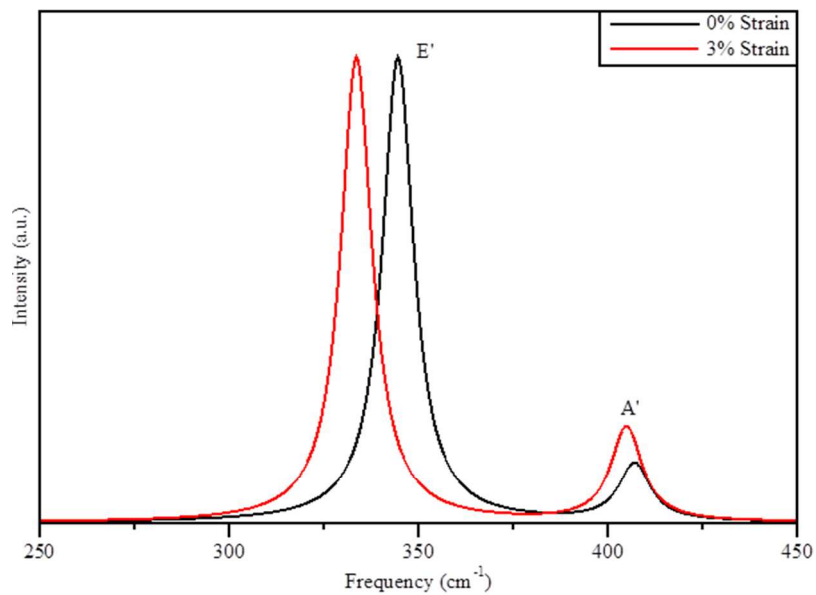


Figure S4 – Raman peaks for WS₂ generated using a Gaussian smearing with the A' and E'

modes labelled. As it can be seen both modes decrease in frequency with applied strain whilst the intensity increases.

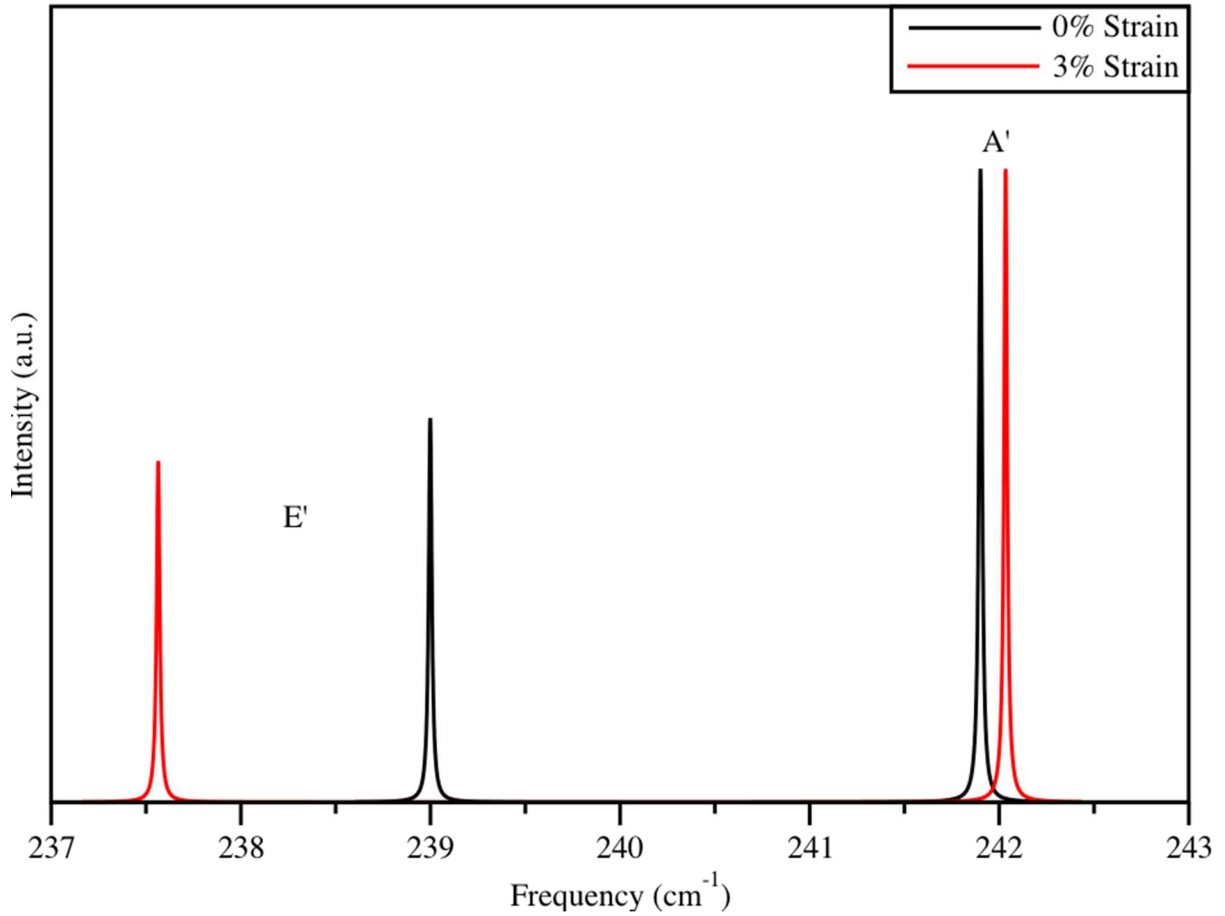


Figure S5 – Raman peaks for WSe₂ generated using a Gaussian smearing with the A' and E' modes labelled. It can be seen that the e' mode decreases in frequency with applied strain whereas the A' mode increases in frequency. Both modes decrease in intensity with applied strain.

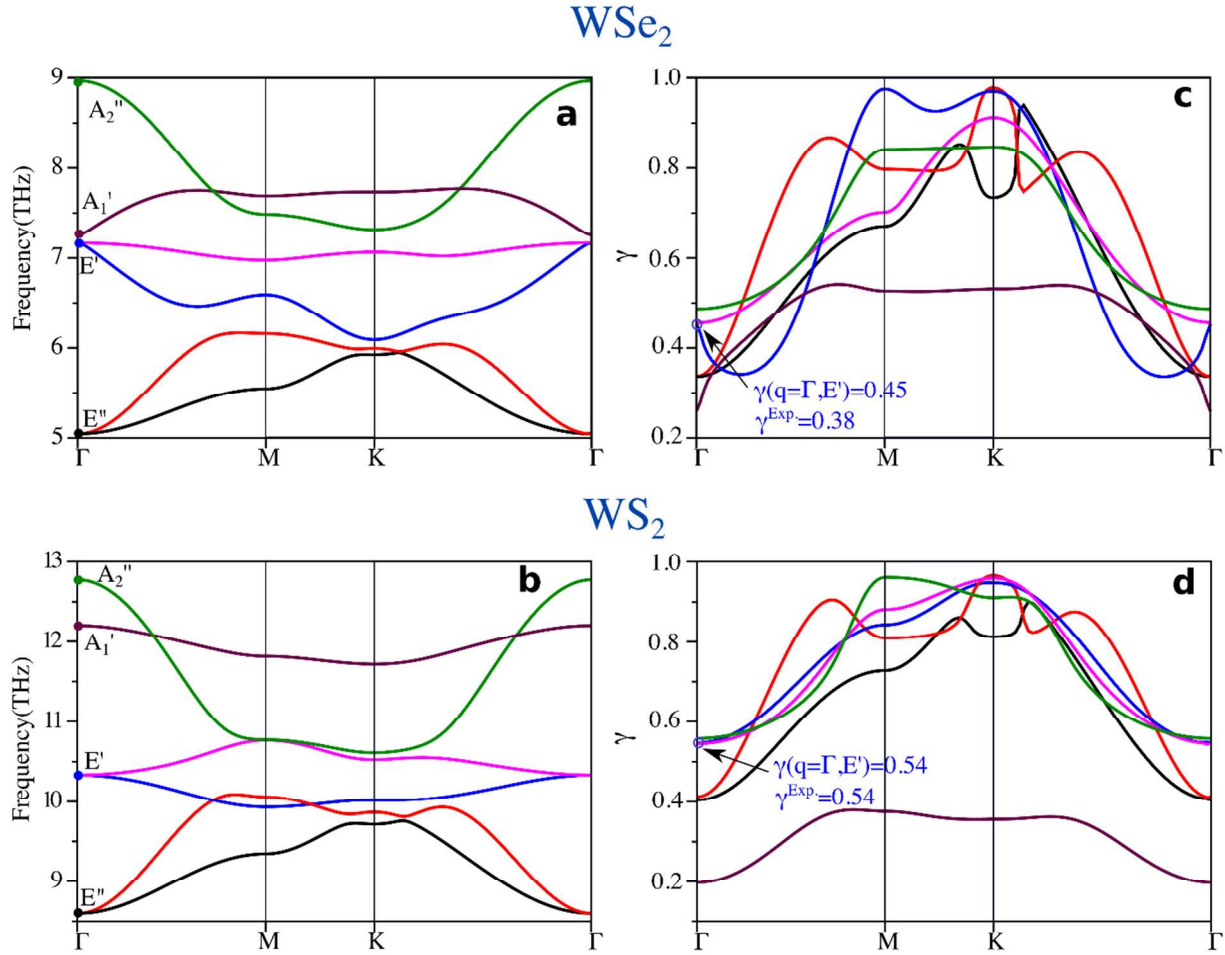


Figure S6 – (a,b) Phonon dispersion branches for optical modes (A_2'' , A_1' , E' , E'') and their respective (c,d) Grüneisen parameters γ calculated along of Γ – M – K – Γ path for monolayer WSe_2 and WS_2 . Modes are labeled according to their symmetries at Γ –point (filled dots) in a and b. The different colors correspond to different phonon branches, which follow the same labeling for γ . At Γ –point, the calculated values of the Grüneisen parameters are $\gamma=0.45$ and $\gamma=0.54$ for WSe_2 and WS_2 , respectively. This is in remarkable agreement with the experimental results $\gamma_{Exp.}=0.38$ (WSe_2) and $\gamma_{Exp.}=0.54$ (WS_2).

Photoluminescence spectra of monolayer films

To check the effect of the bonding process on the electronic structure of the monolayer films, we performed photoluminescence (PL) spectroscopy during the bonding process for both WSe₂ and WS₂. PL spectra were obtained with the identical experimental setup as used for the Raman spectroscopy measurements discussed in the main text. The results are shown in figure S7. Spectra taken in the as-grown state and after bonding show the prominent excitonic peak that is observed commonly for these monolayers. In the as-grown state, the monolayer films are under compressive strain due to differential thermal expansion, which causes a red shift in the spectrum by about 100 meV. This strain is released upon removal of the film from the SiO₂ substrate. Additionally, we find that the band width of the PL spectra increases by about 20 meV after release in comparison to the as-grown films. The widths of the PL spectra we observe before and after bonding are comparable to other CVD-grown films reported previously¹⁰. The process of bonding of the released film does not introduce additional changes to the PL spectrum, indicating that the bonding process itself does not cause deterioration in the quality of the film.

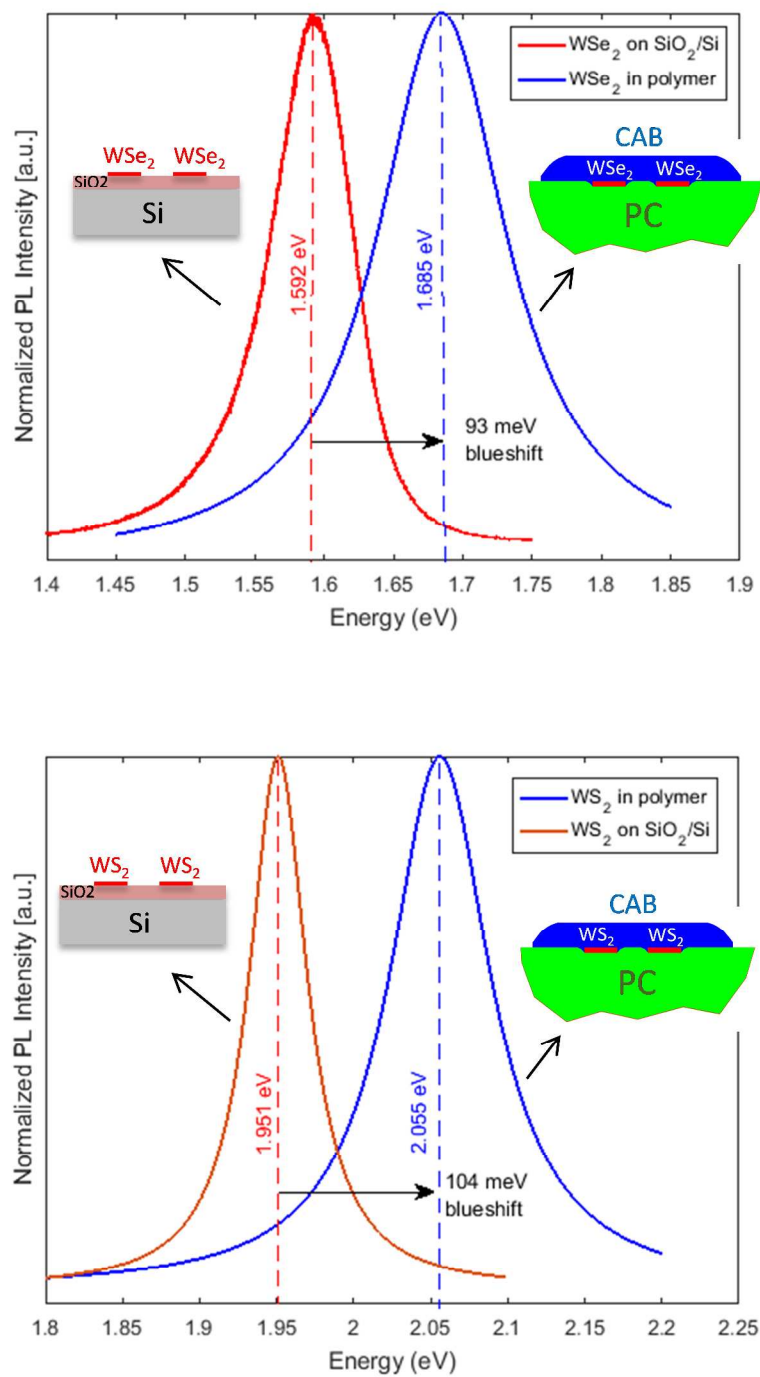


Figure S7– Photoluminescence (PL) of WSe₂ (above) and WS₂ (below) before and after transfer. PL signals are normalized to their peak intensities for better illustration

REFERENCES

1. Timoshenko, S., History of Strength of Materials. **1953**.
2. Loudon, R., Raman effect in crystals. *Adv. Phys.* **1964**, 13, 423-482.
3. Kresse, G.; Hafner, J., Ab initio. *Phys. Rev. B* **1993**, 48, 13115-13118.
4. Kresse, G.; Furthmüller, J., Efficient iterative schemes for ab initio total-energy calculations using a plane-wave basis set. *Phys. Rev. B* **1996**, 54, 11169-11186.
5. Parlinski, K.; Li, Z. Q.; Kawazoe, Y., First-Principles Determination of the Soft Mode in Cubic ZrO₂. *Phys. Rev. Lett.* **1997**, 78, 4063-4066.
6. K., P., Software PHONON. *Cracow* **2010**.
7. Perdew, J. P.; Burke, K.; Ernzerhof, M., Generalized Gradient Approximation Made Simple. *Phys. Rev. Lett.* **1996**, 77, 3865-3868.
8. Blöchl, P. E., Projector augmented-wave method. *Phys. Rev. B* **1994**, 50, 17953-17979.
9. Kresse, G.; Joubert, D., From ultrasoft pseudopotentials to the projector augmented-wave method. *Phys. Rev. B* **1999**, 59, 1758-1775.
10. Liu, B.; Fathi, M.; Chen, L.; Abbas, A.; Ma, Y.; Zhou, C., Chemical Vapor Deposition Growth of Monolayer WSe₂ with Tunable Device Characteristics and Growth Mechanism Study. *ACS Nano* **2015**, 9, 6119-6127.